Energy & Environmental Science

PAPER

View Article Online
View Journal

Cite this: DOI: 10.1039/c7ee03245e

Isolated Ni single atoms in graphene nanosheets for high-performance CO_2 reduction†

Kun Jiang, ‡[a] Samira Siahrostami,‡[b] Tingting Zheng,[ac] Yongfeng Hu,[d] Sooyeon Hwang,[e] Eli Stavitski,[f] Yande Peng,[ag] James Dynes,[d] Mehash Gangisetty,[a] Dong Su,[e] Klaus Attenkofer[f] and Haotian Wang *[a]

Received 14th November 2017,
Accepted 1st February 2018

DOI: 10.1039/c7ee03245e

rsc.li/ees

Single-atom catalysts have emerged as an exciting paradigm with intriguing properties different from their nanocrystal counterparts. Here we report Ni single atoms dispersed into graphene nanosheets, without Ni nanoparticles involved, as active sites for the electrocatalytic CO_2 reduction reaction (CO_2RR) to CO. While Ni metal catalyzes the hydrogen evolution reaction (HER) exclusively under CO_2RR conditions, Ni single atomic sites present a high CO selectivity of 95% under an overpotential of 550 mV in water, and an excellent stability over 20 hours' continuous electrolysis. The current density can be scaled up to more than 50 mA cm^{-2} with a CO evolution turnover frequency of 2.1×10^5 h^{-1} while maintaining 97% CO selectivity using an anion membrane electrode assembly. Different Ni sites in graphene vacancies, with or without neighboring N coordination, were identified by *in situ* X-ray absorption spectroscopy and density functional theory calculations. Theoretical analysis of Ni and Co sites suggests completely different reaction pathways towards the CO_2RR or HER, in agreement with experimental observations.

Broader context

Electrocatalytic CO_2 reduction under ambient conditions has provided a promising route to use renewable electricity for delocalized energy storage and chemical production applications. However, this process is currently challenged by its low selectivity and activity, especially the strong competitions from H_2 evolution in aqueous solutions. Most of the transition metals, except for the few well-known catalysts such as Au, Ag, and Cu, intend to reduce H_2O instead of CO_2 under a significant overpotential. However, once those metals are dispersed into their single-atom morphology, their catalytic behaviors could be dramatically shifted. Herein, we explored different transition metal single-atom catalysts in graphene nanosheets for highly selective CO_2 reduction, with comparable performance to noble metal catalysts. More importantly, an anion membrane electrode assembly was demonstrated to prevent the direct contact between the catalyst and liquid water, maximally suppressing the H_2 evolution side reaction and facilitating the CO_2 mass transport, under significant overpotentials which are required for scale-up currents in real applications in the future.

Introduction

Converting CO_2 into chemicals or fuels using green electricity under mild conditions has attracted intensive attention as it begins to receive driving forces from both environmental protection and market economies.[1–7] Due to the relatively stable nature of CO_2 gas, significant overpotentials (a few hundreds of millivolts) are usually needed to overcome the activation barriers and deliver reasonable currents, under which, however, the side reaction (hydrogen evolution reaction (HER)) can easily take off on a variety of catalytic materials. Therefore, a selective catalyst should exhibit appropriate electronic properties which not only favor the CO_2 reduction reaction (CO_2RR) pathway, but can also dramatically suppress the competitive HER. This has been demonstrated in transition metal (TM) catalysts such as Au or Ag with high CO_2-to-CO selectivity,[8–14] which is due to their unique electronic structure that largely suppresses HER kinetics but maintains

[a] Rowland Institute, Harvard University, Cambridge, MA 02142, USA. E-mail: hwang@rowland.harvard.edu
[b] SUNCAT Center for Interface Science and Catalysis, Department of Chemical Engineering, Stanford University, Stanford, CA 94305, USA
[c] Hefei National Laboratory for Physical Sciences at the Microscale, University of Science and Technology of China, Hefei 230026, China
[d] Canadian Light Source Inc., University of Saskatchewan, 44 Innovation Boulevard, Saskatoon, SK, S7N 2V3, Canada
[e] Center for Functional Nanomaterials, Brookhaven National Laboratory, Upton, New York 11973, USA
[f] National Synchrotron Light Source II, Brookhaven National Laboratory, Upton, New York 11973, USA
[g] Department of Chemistry, University of Science and Technology of China, Hefei 230026, China

† Electronic supplementary information (ESI) available: Additional (S)TEM, XPS, and XAS characterization data; CO_2RR performance evaluation of control samples; CO evolution kinetic analysis; calculation of the turnover frequency per Ni site; free energy diagrams of CO_2 to CO conversion; and electrochemical performance comparison with reported non-noble catalysts. See DOI: 10.1039/c7ee03245e

‡ These authors contributed equally to this work.

weak CO binding for a facile desorption. However, low-cost, earth-abundant catalytic materials for the high-performance CO_2RR need to be extensively explored to replace those noble metals for both fundamental studies and practical applications.[15–23]

Early group TMs such as Fe, Co and Ni, with good HER activities and poor resistances to CO-poisoning (strong surface bonding), were rarely selected as promising electrocatalyst candidates for CO_2-to-CO conversion. However, their electronic structures can be significantly modified once dispersed into single atoms,[24–32] leading to several beneficial properties for catalysis applications. Firstly, the single atoms exhibit spectacular stability due to the strong chemical bonding between the single metal atoms and substrate.[33] Secondly, due to the confinement of electrons, discrete energy levels are formed around the Fermi level, which is a direct consequence of quantum size effects.[34] Lastly, the unsaturated coordination environment of the metal single atom provides a fascinating active center with intriguing properties for catalysis.[35,36] One representative example is the Co porphyrin structure, in line with earlier metal–cyclam studies,[37–39] where a single Co atom coordinated with four neighboring N, that exhibits high selectivity towards CO evolution in a sharp contrast to Co metal which generates hydrogen exclusively.[40–42] Therefore, studying the electronic properties of different TM atoms in varied coordination environments, and exploring effective methods to incorporate single atoms into an appropriate matrix material, could provide new insights and design principles in developing highly selective CO_2RR catalysts using those low-cost materials. Two-dimensional layered materials, such as graphene, have well-defined atomic structure and a variety of chemical coordination environments to tune the electronic properties of confined intra-layer guest atoms.[43–47] Previous works have demonstrated the successful incorporation of Ni single atoms into the vacancies of a defective graphene shell, where an underneath Ni nanoparticle (NP) is tightly wrapped, by mixing Ni and C precursors together followed by heat treatment.[30] However, this core–shell structure suffers from a few disadvantages: (1) the existing Ni NPs can heavily generate H_2 once the graphene shell has pin holes or is broken during electrolysis; (2) only a small fraction of Ni atoms participate in catalytic reactions but most of them are buried as Ni NPs; (3) the complicated core–shell structure brings challenges in characterizing the single atoms and their coordination, due to the dominating metallic signals contributed by Ni NPs; and (4) the coordination environment of single atoms and the density of surface active sites cannot be well controlled. Therefore, different methods to controllably confine single atoms into graphene vacancies are highly desired to effectively tune the TM electronic structures for selective CO_2-to-CO conversion. While different TM single atoms can be confined into a similar coordination environment, their CO_2RR selectivity can spread over a wide range due to their varied band structures. Due to the competitive relationship between the CO_2RR and HER, theoretical analysis of HER activities on those single atomic sites needs to be detailed, in addition to the traditionally studied CO_2 activation and CO desorption barriers, for a more comprehensive understanding and accurate guidance of site selectivity.

Here we report Ni single atoms uniformly dispersed in a two-dimensional (2D) graphene layer as highly active and selective centers for electrocatalytic CO_2 to CO conversion. The single atom morphology and atomic coordination were identified by aberration-corrected scanning transmission electron microscopy (STEM) and *operando* X-ray absorption spectroscopy (XAS). As a result, more than 90% of CO selectivity was delivered within a wide electrochemical potential window in aqueous solution, with a maximal CO Faradaic efficiency (FE) of more than 95% under an overpotential of 550 mV. The single Ni atomic sites also present excellent stability to maintain a stable CO selectivity of $\sim$90% for over 20 hours' continuous electrolysis. A CO evolution current of more than 200 mA (50 mA cm^{-2}) under a 97% FE was demonstrated on a 4 cm^2 anion membrane electrode assembly using earth-abundant catalytic materials. Other TM atomic sites such as Co, Fe, and Mn exhibit different reaction pathways, especially for Co which generates hydrogen exclusively. Density functional theory (DFT) calculations suggest that the weaker CO binding and higher HER barrier account for the superior CO_2-to-CO selectivity of Ni single atoms than that of Co.

Results

Preparation and characterization of Ni single atom catalyst

Layered graphene oxide (GO) nanosheets were selected as the matrix material for Ni single atoms for the following reasons: (1) a high density of defects was created in GO; (2) the large-area, negatively-charged surface helped in uniformly absorbing a monolayer of positive metal cations for single atom dispersion; (3) the density of single atom active sites could be maximized on the 2D surface for higher catalytic activities; and (4) the single atomic site could be clearly characterized on the well-defined 2D structure. We first of all controllably incorporated a small amount of Ni ions into GO nanosheets, after which the mixture was annealed under 750 °C with ammonia as the reducing reagent and the source of N dopants (Experimental). Atomically dispersed Ni atoms coordinated in graphene vacancies (Ni–NG) were obtained as shown in Fig. 1 and Fig. S1 (ESI†). While no Ni NPs or clusters were observed in the 2D Ni–NG nanosheet in Fig. 1A by transmission electron microscopy (TEM), the elemental mapping (Fig. 1D) by energy-dispersive X-ray spectroscopy (EDS) suggests the existence and uniform distribution of Ni atoms. The atomic ratio was determined to be $\sim$0.44 at% by X-ray photoelectron spectroscopy (XPS, Fig. S2, ESI†), consistent with the estimation from material synthesis (Experimental). Aberration-corrected high-angle annular dark-field scanning transmission electron microscopy (HAADF-STEM) with Z-contrast can differentiate Ni atoms from the surrounding light elements for detailed characterization (Experimental). Ni atoms with high contrast were observed to be homogeneous on the graphene layer (Fig. 1B), which under a higher magnification suggests an atomically dispersed morphology in Fig. 1C. The red circles point out a few representative single Ni atoms in graphene.

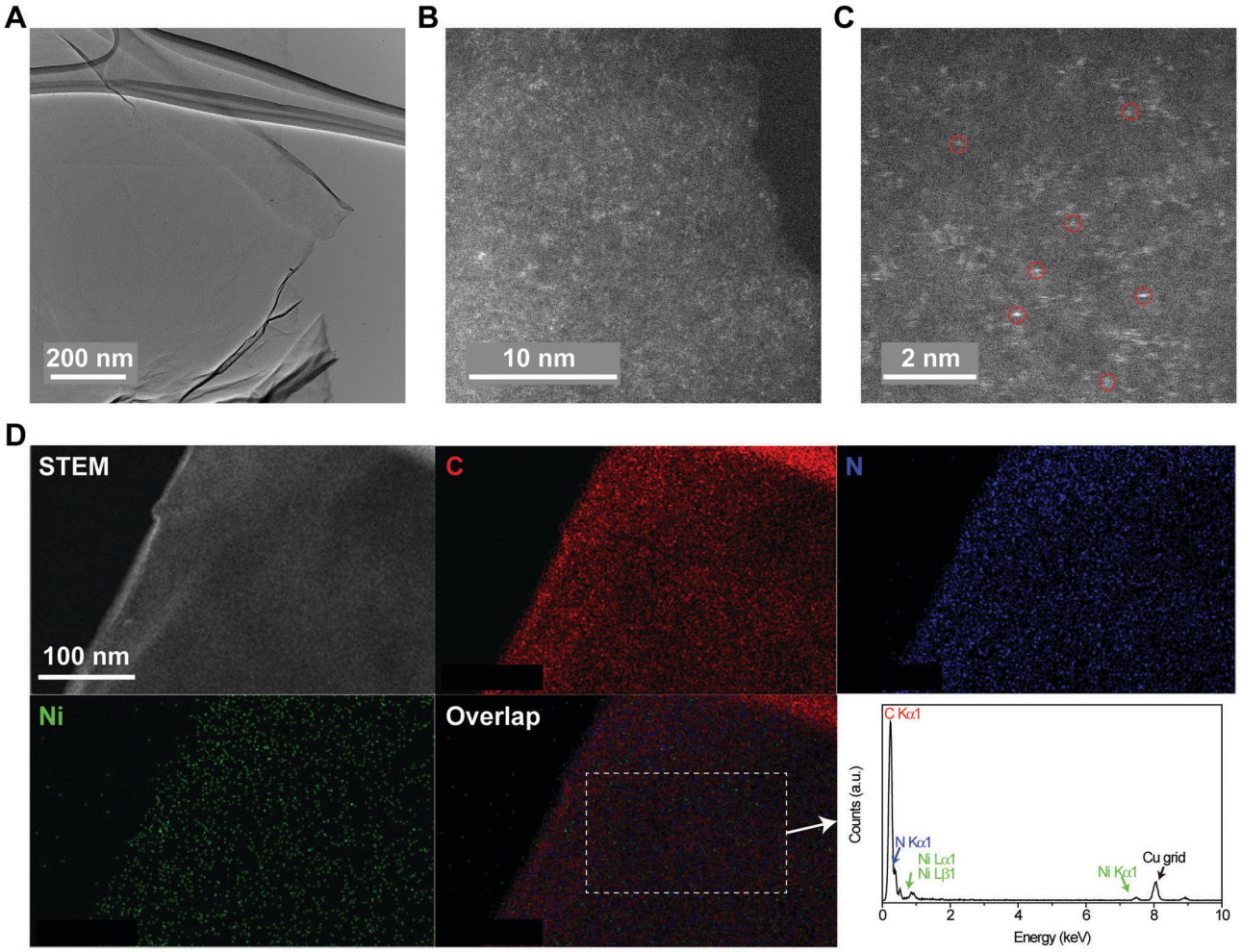

Fig. 1 Morphology and composition characterization of Ni–NG. (A) TEM image of a Ni–NG nanosheet. No Ni NPs were observed. (B) Aberration-corrected HAADF-STEM image of a Ni–NG nanosheet. The uniformly distributed bright dots represent Ni atoms due to the high mass compared to C or N. (C) A zoom-in STEM image of Ni–NG. Isolated Ni single atoms (brighter dots) were observed, and a few representatives were indicated by red circles. (D) Elemental mapping of a Ni–NG nanosheet confirming the co-existence of C, N, and Ni atoms.

Electrocatalytic CO_2RR performance

The CO_2RR catalytic activity of the Ni–NG catalyst, drop-cast onto a mirror polished glassy carbon electrode (GCE), was evaluated in a standard three-electrode H-cell configuration with CO_2-saturated 0.5 M $KHCO_3$ as the electrolyte (Experimental). H_2 and CO are the major gas products detected by on-line gas chromatograph (Experimental), with their FEs under different potentials and the corresponding partial currents shown in Fig. 2A and B, respectively. CO_2-to-CO conversion starts from -0.31 V *vs.* RHE ($\sim$190 mV overpotential), which rapidly increases to an 83% of the CO FE at an overpotential of 480 mV, and maintains a high plateau of more than 90% CO until -0.87 V. The competitive HER was dramatically suppressed with FEs less than 10%, in sharp contrast to the supported Ni nanoparticle catalyst (Fig. S3 and S4, ESI†). The Tafel slope (Fig. S5, ESI†), which is used to analyze the kinetic behavior of the CO_2RR on Ni single atomic sites, is $\sim$110 mV dec^{-1} and comparable to Au- and Ag-based electrocatalysts,[9,48] suggesting a rate-limiting step of the initial CO_2 activation.[30,49] The CO production turnover frequency (TOF) per active Ni site is calculated to be 6.8 s^{-1} at an overpotential of 0.57 V, based on electrochemical surface area determination from double layer capacitance measurements (Fig. S6, ESI†), and increases to 21.2 s^{-1} at an overpotential of 0.75 V. The geometrical current density can be further improved with a high surface area current collector (carbon fiber paper, CFP) and more mass loading of catalysts (1 mg cm^{-2}). Compared to the CO_2RR performance on the GCE, the current density was significantly improved while maintaining a similar trend of CO selectivity. A maximal CO FE of $\sim$95% (Fig. 2C) with a current density of $\sim$11 mA cm^{-2} was achieved under an overpotential of 620 mV (Fig. 2D). It is noted that the current density was not linearly improved with catalyst loading, which is possibly due to the overlap of graphene layers on CFP. Long term CO_2RR stability is a particularly important measure for single atom catalysts due to the potential atom aggregation during catalysis. The Ni–NG catalyst maintains a stable current density of $\sim$12 mA cm^{-2} and a CO selectivity of $\sim$90% for more than 20 hours' continuous operation, demonstrating an excellent electrocatalytic durability.

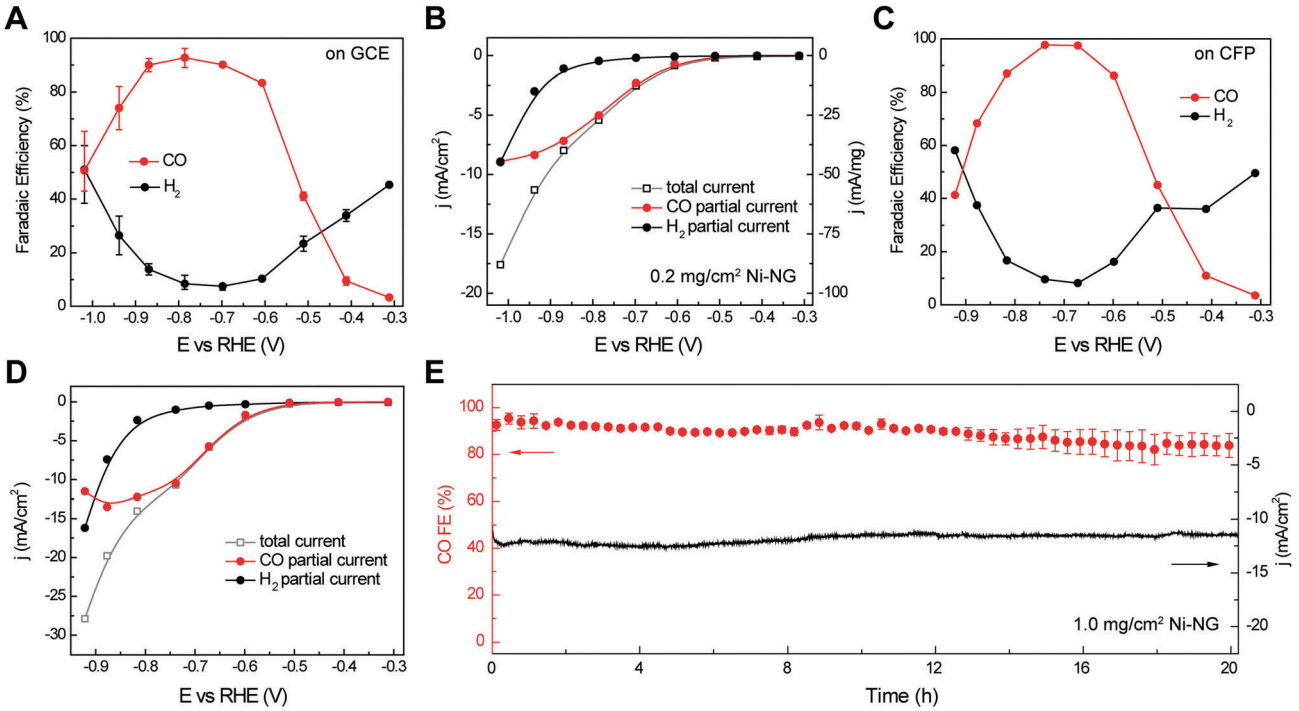

Fig. 2 Electrocatalytic CO_2RR performance of Ni–NG in a H-cell. (A and B) FEs of H_2 and CO and the corresponding steady-state current densities of Ni–NG on a GCE in CO_2-saturated 0.5 M $KHCO_3$. The catalyst mass loading is 0.2 mg cm^{-2}. The error bars represent three independent samples. (C and D) FEs of H_2 and CO and the corresponding steady-state current densities of Ni–NG on CFP in CO_2-saturated 0.5 M $KHCO_3$. The catalyst mass loading is 1 mg cm^{-2}. All gas products were sampled into on-line GC after a continuous electrolysis of ~15 min under each potential. (E) The CO_2RR stability test of the current density and CO FE of Ni–NG on CFP under an overpotential of 0.64 V for more than 20 h continuous operation. The error bars represent two independent samples.

Those Ni atoms largely maintain the isolated feature as observed in the post-catalysis TEM image and X-ray fine structure characterization (Fig. S7, ESI†), suggesting the stable confinement of Ni single atoms in graphene vacancies. Besides, the electrolyte before and after 20 h electrolysis was examined by inductively coupled plasma atomic emission spectroscopy; no detectable Ni species was observed (detection limit of ~100 ppb) in both cases, suggesting a negligible Ni leaching.

We noticed that the CO evolution current on the Ni–NG catalyst was limited in the H-cell system. Due to the direct contact between the catalyst and water, the HER would easily take off under a significant overpotential needed to boost the current (Fig. 2B and D). An anion membrane electrode assembly (MEA) can prevent the catalyst from contacting with water and also facilitate the CO_2 mass transport (Fig. 3A, Experimental),[50–52] greatly suppressing the competing HER even under large overpotentials. More than 200 mA current was achieved on a 4 cm^2 electrode for demonstration (50 mA cm^{-2}), with a high CO selectivity of ~97% and H_2 of only ~4% (Fig. 3B and C). Fig. 3D exhibits a stable CO selectivity of >90% under a significant current of ~200 mA (50 mA cm^{-2}) over the 8 h continuous electrolysis, which represents an unprecedented CO evolution rate of 3.81 mmol h^{-1} using earth-abundant electrocatalysts (Table S1, ESI†) and a record TOF of ~59 s^{-1} (or ~2.1×10^5 h^{-1}) at a cell voltage of 2.78 V. More than 630 mL of CO gas was accumulated during this electrolysis (Fig. 3E), which can be further scaled up in real applications by extending the size of the gas diffusion layer, increasing the catalyst loading, or by stacking multiple cells together.

To better probe the active sites in Ni–NG toward this superb CO_2RR performance, control experiments on Ni-coordinated graphene without the incorporation of N (Ni–G), N-doped graphene (NG) and Ni_3N catalysts were carried out and are shown in Fig. S8 and S9 (ESI†) (Experimental). First of all, the possibility that the Ni_3N compound will be responsible for the high CO selectivity on the Ni–NG catalyst was ruled out due to the extensive observed HER (H_2 FE is ~80%). In addition, NG without the incorporation of Ni atoms showed a poor CO_2-to-CO selectivity, suggesting that neither the N dopants nor metal impurities[53] (if any) in graphene (the XPS survey in Fig. S10 (ESI†) and energy dispersive X-ray spectrum in Fig. S11 (ESI†) suggest a negligible metallic impurity) directly contribute to the high CO selectivity of Ni–NG. Finally, without the incorporation of N, the Ni–G catalyst exhibited a maximal CO FE of ~41% at −0.80 V. This reasonable selectivity agrees well with our previous demonstration that Ni single atoms coordinated with C in graphene vacancies (Ni@vacancies), such as Ni@SV and Ni@DV, are active sites for CO_2-to-CO conversion. However, when N dopants were incorporated during the synthesis process to obtain a Ni–NG catalyst, the CO selectivity was further boosted with a greatly suppressed HER. More structure and coordination information about Ni–G and Ni–NG catalysts is necessary to understand the critical role of N dopants, and whether the active sites of Ni–C coordination have been changed.

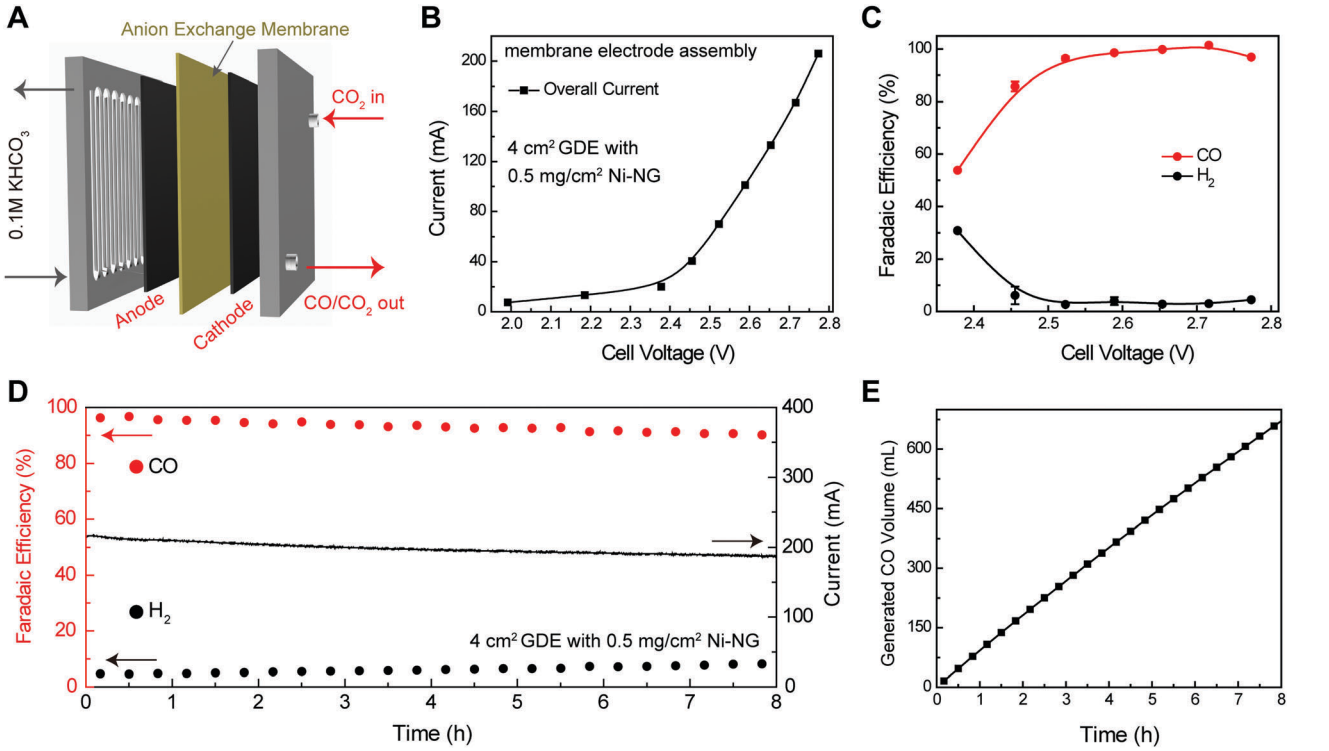

Fig. 3 Electrocatalytic CO_2RR performance on the Ni–NG catalyst by anion membrane electrode assembly. (A) Schematic of the anion MEA, with a cathode of Ni–NG for the CO_2RR and an anode of IrO_2 for the oxygen evolution reaction. The Ni–NG catalyst does not directly contact with liquid electrolyte. (B) The steady-state current of Ni–NG (0.5 mg cm^{-2}) on the 4 cm^2 electrode and (C) the corresponding FEs of H_2 and CO. The error bars represent three independent samples. (D) Long-term electrolysis under a full-cell voltage of 2.78 V, showing a stable current of ~200 mA (~50 mA cm^{-2}). The CO selectivity maintained above 90% over the course of 8 h continuous operation. (E) The accumulated CO production during the 8 h continuous electrolysis.

Electronic structure and coordination environment analysis

Ex situ and *in situ* X-ray characterization studies were performed to further probe the atomic and electronic structures of Ni single atomic sites and their surrounding coordination environment. The XPS study of Ni–NG and Ni–G in Fig. S12A (ESI†) shows positive Ni $2p_{3/2}$ binding energies than Ni metal (852.6 eV),[54] suggesting the positive oxidation states of Ni single atoms in different coordination environments. In addition, the Ni 2p binding energy of Ni–NG is slightly higher than that of Ni–G (Ni–C coordination), indicating the possible Ni–N coordination which further levels up the Ni oxidation states.[30,55] The coordination environment of Ni atomic sites can be extensively studied using synchrotron-based X-ray absorption spectroscopy (XAS). Fig. 4A shows the typical X-ray absorption near-edge structure (XANES) spectrum of the Ni K-edge in the Ni–NG catalyst, with Ni metal and NiO as references (see also Fig. S13, ESI†). The near-edge of Ni–NG sits in between Ni metal and NiO, indicating that the average oxidation states of those Ni single atoms are between the metallic and the fully oxidized states. This is because the neighboring C (or possibly N) atoms partially deplete Ni free electrons through the valence bond, as shown in the simulated charge density distribution (Fig. 4B). The *in situ* XAS test of Ni–NG during the CO_2RR electrolysis shows no obvious changes in Ni XANES under different potentials applied (Fig. 4C), suggesting the high stability of Ni single atoms confined in graphene vacancies and thus ensuring a practical use in long-term electrolysis.

The possible coordination environment around Ni single atoms was further analyzed using the k^2-weighted Fourier transforms of the extended X-ray absorption fine structure (EXAFS) at the Ni K-edge in Fig. 4D, where the Ni–NG catalyst and other model references such as Ni phthalocyanine (Ni–Pc, Fig. S14, ESI†) were included. Ni metal exhibits a typical first shell Ni–Ni pair at ~2.20 Å, while Ni–O interaction in NiO locates at 1.62 Å. The *R*-space characteristics of Ni–N bonding can be studied using Ni–Pc due to its well-defined structure, which suggests a 1.40 Å bonding length of Ni–N. Ni–G exhibits a distinguished peak, assigned as Ni–C coordination, at the same position of 1.40 Å, suggesting that it is difficult to fully differentiate Ni–C and Ni–N coordination due to their very close bonding lengths.[26,28] In addition, another peak at ~2.06 Å indicates the possible presence of Ni–Ni bonding from small Ni clusters, which is consistent with STEM observations in Fig. S15A (ESI†). The coexistence of Ni single atoms in graphene vacancies and Ni clusters explains the comparable CO_2RR and HER processes on Ni–G (Fig. S8, ESI†), and further confirms the CO_2-to-CO activity on atomic sites of Ni@vacancies (Fig. 5A). When N dopants were introduced during the sample synthesis, the morphology and coordination environment of Ni atoms changed. Different from Ni–G, our Ni–NG catalyst shows negligible Ni–Ni

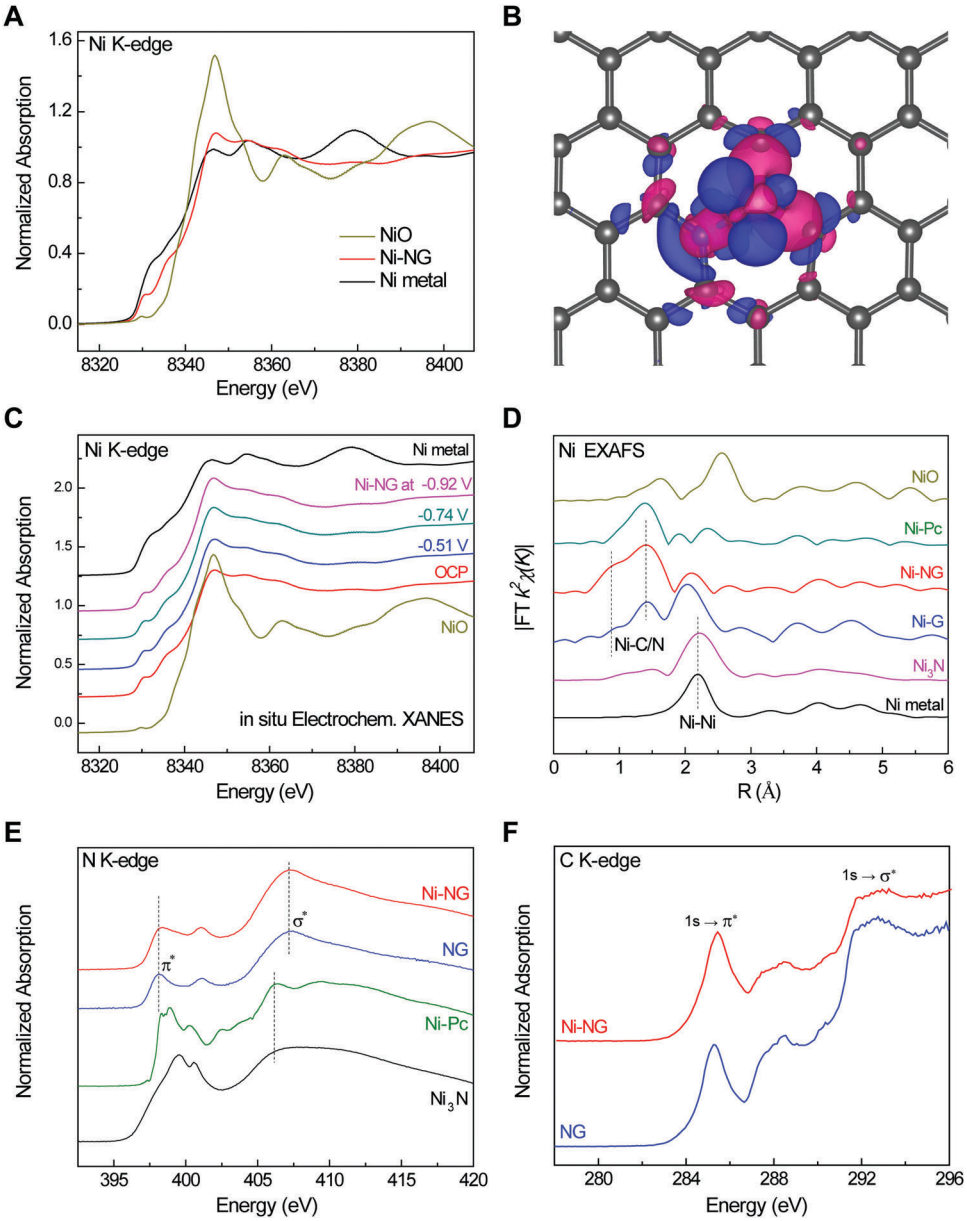

Fig. 4 XAS characterization of Ni–NG catalysts and control samples. (A) Ni K-edge XANES of the Ni–NG catalyst and Ni metal and NiO as the references. (B) Charge density distribution of the Ni single atoms confined in graphene vacancies (Ni–NG in single vacancy configuration, *vide infra*). Blue and magenta represent electron accumulation and depletion, respectively. The pronounced delocalization observed in both charge density difference plots indicates a strong interaction and a significant charge transfer between coordinated C or N atoms and single Ni atoms. (C) *In situ* electrochemical XANES spectra of Ni–NG under different potentials during CO_2RR electrolysis. (D) Ni K-edge Fourier transformed EXAFS spectra in the *R* space of the Ni–NG catalyst in comparison to other Ni-based control samples. (E) N K-edge and (F) C K-edge XAS spectra for Ni–NG and reference samples.

interaction with most of the Ni atoms in the single atomic morphology as suggested by EXAFS (Fig. 4D). In addition, the XANES and EXAFS of both Ni and N in Ni–NG show distinguished differences from that of Ni–Pc, ruling out the possibility that those single Ni atoms are coordinated with N only such as a Ni porphyrin structure, and thus suggesting a mixed Ni–C and Ni–N coordination environment.[26] Since there are a variety of different sizes of vacancies in graphene oxide nanosheets due to their violent synthesis process,[56] it is believed that different types of Ni atomic sites could exist. Small vacancies such single vacancies (SV) or double vacancies (DV) with one or two C atoms missing can fit a single Ni atom for Ni@vacancy active sites (Fig. 5A).[30] For slightly larger vacancies, due to their more negative surface charges, they could adsorb more Ni ions and thus result in small Ni clusters in the Ni–G catalyst in the absence of N dopant. Our assumption is that the incorporation of N could potentially help in isolating the Ni atoms by forming Ni–N in addition to Ni–C bonds in the Ni–NG catalyst, with representative atomic sites such as Ni–N@SV or Ni–N@DV illustrated in Fig. 5A.[30] A more clear comparison of the Ni–Ni

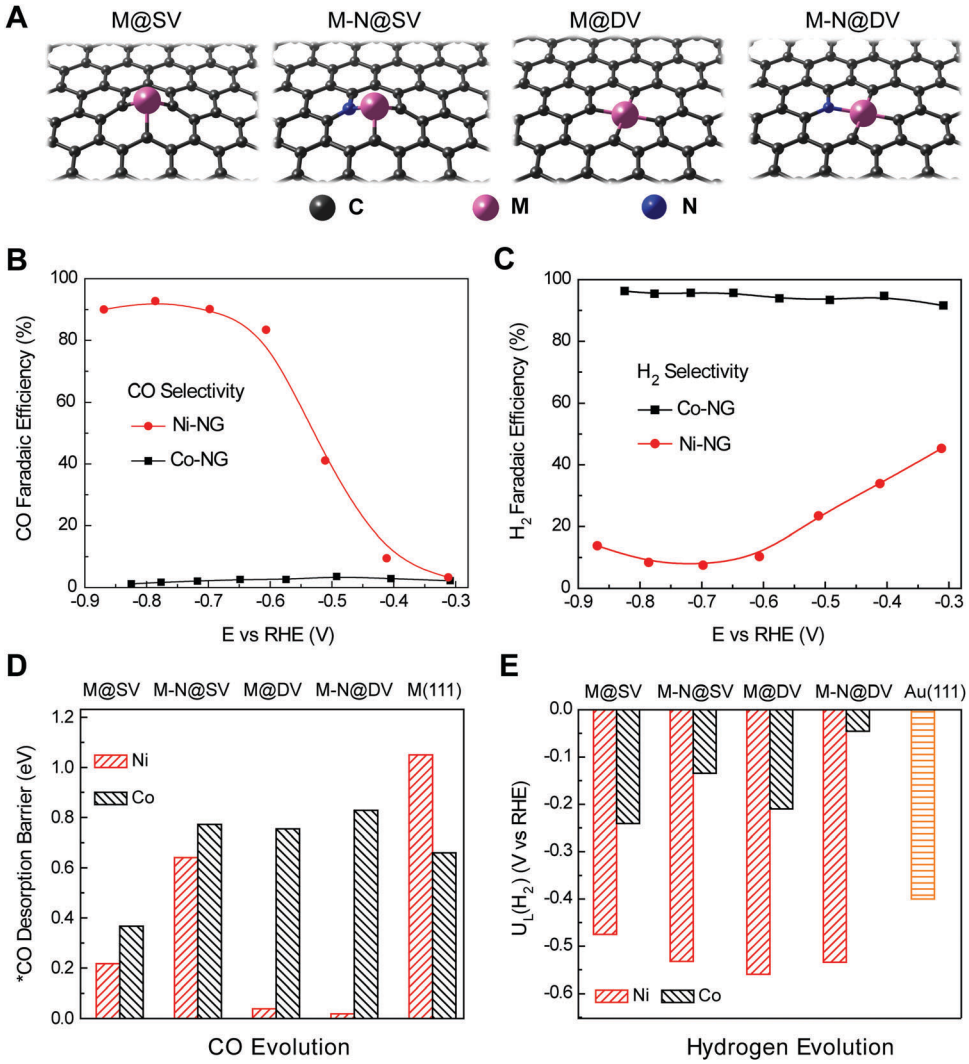

Fig. 5 Electrocatalytic selectivity toward the CO_2RR and HER over Ni–NG *vs.* Co–NG catalysts. (A) Different atomic configurations in a graphene matrix for metal–carbon and/or metal–nitrogen–carbon coordination. (B) CO and (C) H_2 Faradaic efficiencies recorded at different potentials over Ni–NG and Co–NG cast glassy carbon electrodes within 0.5 M $KHCO_3$. (D) The adsorbed desorption barrier diagram for *CO and (E) the limiting potential diagram for the HER on model systems.

pair intensities in EXAFS patterns between Ni NPs loaded onto graphene nanosheets (Ni NPs/G) and Ni–G and Ni–NG samples is shown in Fig. S15B (ESI†). The Ni–Ni bonding was dominant in Ni NPs/G, which was significantly weakened in the Ni–G sample with the coexistence of the Ni–C signal, and was further eliminated in the Ni–NG sample with a dominant Ni–C/N peak. As a result, the Ni NPs generate exclusively H_2 (Fig. S4, ESI†), Ni–G presents nearly 40% selectivity of CO_2 reduction (Fig. S8, ESI†), and Ni–NG shows more than 95% CO selectivity (Fig. 2). This trend provides strong evidence that the Ni single atomic sites are responsible for CO_2 reduction. Furthermore, the N K-edge XAS spectrum of Ni–NG exhibits strong signals in both π^* (398.1 eV) and σ^* (407.2 eV) bands, which is similar to NG (Fig. 4E) but different from Ni–Pc and Ni_3N, indicating that the majority of N dopants are coordinated with carbon to form pyridine- and pyrrole-ring structures (Fig. S12B, ESI†).[27] Additional C K-edge XAS spectra of Ni–NG and NG (Fig. 4F) show similar graphene matrix structures as evidenced by similar π^* band intensities at ~285.4 eV, but more defects within the macrocyclic pyrrolic carbon structure in the Ni–NG catalyst.[27,57]

Discussion

The critical role of Ni atoms in catalyzing CO_2-to-CO conversion was further confirmed when replaced by other TMs including Fe, Co, Mn, and Cu, which exhibit dramatically decreased selectivity (Fig. S16 and S17, Experimental, ESI†). Among all of these control metals, the Co–NG catalyst, with only one d-orbital electron less than Ni counterpart, is of particular interest due to its excellent HER performance in a sharp contrast to the Ni–NG catalyst (Fig. 5B, C and Fig. S17, ESI†). The high CO and low H_2 selectivities on Ni–NG were completely reversed on Co–NG, although the STEM and EXAFS characterization of Co–NG

confirms the atomically dispersed Co morphology (Fig. S18, ESI†). Therefore, theoretical analysis of the electronic structure change, as well as its effects on both the CO_2RR and HER, not only provides key insights into understanding this significantly different selectivity, but could also further validate the coordination structure of those single atom active sites. Here we use density functional theory (DFT) to study the elementary reaction steps of the CO_2-to-CO conversion and HER on different atomic metal (Ni or Co) sites shown in Fig. 5A (Experimental).

Thermochemical analysis for the two-electron CO_2-to-CO on TM surfaces suggests that the reaction pathway goes through COOH* and CO* intermediates:[49,58]

$$CO_2 + * + (H^+ + e^-) \rightarrow COOH*$$

$$COOH* + (H^+ + e^-) \rightarrow CO* + H_2O$$

$$CO* \rightarrow CO + *$$

$$\text{Total: } CO_2 + 2(H^+ + e^-) \rightarrow CO + H_2O \quad E^0 = -0.12\ \text{V} \qquad (1)$$

where * represents the active site. For surfaces such as Au and Ag with weak CO* binding, the major product will be CO gas.[58] We therefore use the adsorption energies of CO* and COOH* to estimate the activity towards the two-electron CO_2RR, and the H adsorption energy to capture the HER (Fig. S19, ESI†).[59] For the atomic sites with positive CO* binding energy, the activity towards CO production can be determined exclusively by the COOH* binding strength. An optimal COOH* binding strength, not too weak nor too strong, is desirable in line with the Sabatier principle.[60] As the equilibrium potential for reaction (1) is −0.12 V *vs.* RHE, using thermodynamic considerations alone, the ideal catalyst should have a COOH* binding energy of 0.12 eV at zero applied potential. Fig. S19 (ESI†) shows that the COOH* and CO* binding energies of the M–N–C motifs vary significantly from their corresponding M(111) counterpart. While Ni@SV, Ni–N@SV and all the related Co–N–C motifs exhibit favorable COOH* binding energies for the CO_2RR, they tend to bind CO strongly at an equilibrium potential of $U = -0.12$ V. Since the CO desorption step is independent of the applied potential, these atomic sites are rate-limited by the CO desorption barrier. The thermodynamically calculated CO desorption barriers on both Ni and Co atomic sites are included in Fig. 5D. Ni shows much lower desorption barriers compared to the Co counterparts, suggesting its improved resistance to CO-poisoning. In addition, the analysis of H* adsorption energy, an effective HER descriptor, on Ni and Co atomic sites shown in Fig. 5E indicates their poor and excellent HER activities, respectively.[26] These results thus elucidate the mechanism for the experimentally observed far less selectivity toward the CO_2RR on Co catalyst than that of Ni, which further confirms the structure and coordination of those single atom active sites in the Ni–NG catalyst.

Conclusions

In summary, by isolating TM single atoms into layered graphene nanosheets, catalytic behaviors dramatically different from their bulk counterparts can be achieved. With different types of metal centers ranging from 3d to 5d TMs, as well as the potential tunable coordination environment in a variety of matrix materials such as TM dichalcogenides, BN, black phosphorus, MXenes, and so on, the catalytic properties of single atom catalysts can therefore be tuned over a broad range for important applications of CO_2 reduction and beyond.

Experimental

Material synthesis

A Ni–NG catalyst was prepared by the impregnation and reduction method. A 3 mg mL^{-1} nickel nitrate stock solution was first prepared by dissolving $Ni(NO_3)_2{\cdot}6H_2O$ (Puriss, Sigma-Aldrich) into Millipore water (18.2 MΩ cm). A carbon suspension was prepared by mixing 50 mg of graphene oxide sheets (GO, purchased from CYG and used as received) with 20 mL of Millipore water, and tip sonicated (Branson Digital Sonifier) for 30 min to a homogeneous dispersion. Then 800 μL of Ni^{2+} solution, given a raw Ni : C atomic ratio of ~0.4 at%, was dropwise added into GO solution under vigorous stirring, and quickly frozen in liquid nitrogen. The ice cube was freeze-dried using an RVT4104 lyophilizer (Thermo) at −100 °C and below 0.2 Torr. The as-prepared $Ni(NO_3)_2$/GO powder was heated in a tube furnace to 750 °C under a gas flow of 50 sccm NH_3 (anhydrous, Airgas) + 150 sccm Ar (UHP, Airgas) within 3 h, and kept at the same temperature for another hour before cooling down to room temperature. N doped graphene (NG) was prepared in a similar way but in the absence of the Ni precursor. To prepare Ni atom doped graphene (Ni–G) and graphene supported Ni nanoparticles (Ni NPs/G), a forming gas (5% UHP H_2 balanced with UHP Ar, Airgas) flow was used during the annealing process, and 8 mL of the Ni^{2+} solution was added in the latter case. Other metal–NG (Co, Fe, Cu, Mn) samples were prepared in a similar way to Ni–NG except for various metal salt precursors ($Co(NO_3)_2{\cdot}6H_2O$, $Fe(NO_3)_3{\cdot}9H_2O$, $Cu(NO_3)_2{\cdot}2.5H_2O$ and $Mn(NO_3)_2{\cdot}4H_2O$ (Puriss or ACS Grade, Sigma-Aldrich), respectively).

Material characterization

The STEM characterization in Fig. 1A was carried out using a JEOL ARM200F aberration-corrected scanning transmission electron microscope under 80 kV. All other TEM images were obtained using a JEOL 2100 transmission electron microscope operated under 200 kV. EDS analysis was performed on a JEOL ARM200F at 60 kV, using an EDAX Octane Plus windowless detector. Drift correction was applied during acquisition.

X-ray photoelectron spectroscopy was performed with a Thermo Scientific K-Alpha ESCA spectrometer, using monochromatic Al Kα radiation (1486.6 eV) and a low energy flood gun as a neutralizer. The binding energy of the C 1s peak at 284.6 eV was used as a reference. The Thermo Avantage V5 program was employed for surface componential content analysis and peak fitting for selected elemental scans.

Ex situ XAS spectra on Ni, N and C K-edges were acquired using the SXRMB beamline of the Canadian Light Source.

The SXRMB beamline used a Si(111) double crystal monochromator to cover the 2–10 keV energy range with a resolving power of 10 000. The XAS measurements were performed in fluorescence mode using a 4-element Si(Li) drift detector in a vacuum chamber. The powder sample was spread onto doublesided, conducting carbon tape. Ni foil was used to calibrate the beamline energy. *In situ* electrochemical XAS measurements on the Ni K-edge were carried out at Beamline 8-ID, National Synchrotron Light Source II, Brookhaven National Laboratory, using a Si(111) monochromator and a Lytle detector. For *in situ* spectroelectrochemical tests, continuous CO_2 flow was delivered into a homemade Teflon H-cell filled with CO_2-saturated 0.5 M $KHCO_3$, a Kapton film covered carbon fiber paper (Ni–NG/CFP) working electrode served as the X-ray window for synchrotron radiation. Multistep potential control was used for the *in situ* measurements, with a hold time of ~30 min at each potential for the spectrum acquisition. Analyses of both the near edge (on an energy scale) and extended range (in the *R* space) XAS spectra were performed using Athena software.

Electrochemical measurements

The electrochemical measurements were run at 25 °C in a customized gastight H-type glass cell separated by a Nafion 117 membrane (Fuel Cell Store). A BioLogic VMP3 work station was employed to record the electrochemical response. A certain amount of $KHCO_3$ (99.95%, Sigma-Aldrich) was dissolved in Millipore water to prepare a 0.5 M electrolyte, which was further purified by electrolysis between two graphite rods at 0.1 mA for 24 h to remove any trace amounts of metal ions. In a typical 3-electrode test system, a platinum foil (99.99%, Beantown Chemical) and a saturated calomel electrode (SCE, CH Instruments) were used as the counter and reference electrodes, respectively. A fresh (electrochemically) polished glassy carbon (HTW GmbH, 1 cm × 2 cm), or an O_2 plasma treated CFP (cut into 1 cm × 2 cm, AcCarb MGL270, Fuel Cell Store), was used as the working electrode substrate.

Typically, 5 mg of the as-prepared catalyst was mixed with 1 mL of ethanol and 100 μL of a Nafion 117 solution (5%, Sigma-Aldrich), and sonicated for 20 min to get a homogeneous catalyst ink. 80 μL of the ink was pipetted onto a 2 cm^2 glassy carbon surface (0.2 mg cm^{-2} mass loading), or 400 μL was pipetted onto CFP to a mass loading of 1.0 mg cm^{-2}, which was vacuum dried prior to use. All potentials measured against the SCE was converted to the reversible hydrogen electrode (RHE) scale in this work using E (*vs.* RHE) = E (*vs.* SCE) + 0.244 V + 0.0591 × pH, where the pH values of the electrolytes were determined using an Orion 320 PerpHecT LogR Meter (Thermo Scientific). The solution resistance (R_u) was determined by potentiostatic electrochemical impedance spectroscopy (PEIS) at frequencies ranging from 0.1 Hz to 200 kHz, and manually compensated for as E (*iR* corrected *vs.* RHE) = E (*vs.* RHE) − $R_u \times I$ (amps of average current).

For an anion membrane electrode assembly test, 0.5 mg cm^{-2} Ni–NG and IrO_2 were air-brushed onto two 2 × 2 cm^2 Sigracet 35 BC gas diffusion layer (Fuel Cell Store) electrodes as a CO_2RR cathode and an OER anode, respectively. A PSMIM anion exchange membrane (Dioxide Materials) was sandwiched by the two gas diffusion layer electrodes (Fig. 3A) to separate the chambers. On the cathode side a titanium gas flow channel supplied 50 sccm humidified CO_2, while the anode was circulated with 0.1 M $KHCO_3$ electrolyte at a flow rate of 2 mL min^{-1}. The cell voltages in Fig. 3 were *iR*-corrected.

CO_2RR product analysis

During electrolysis, CO_2 gas (99.995%, Airgas) was delivered into the cathodic compartment containing CO_2-saturated electrolyte at a rate of 50.0 standard cubic centimeters per minute (sccm, monitored by an Alicat Scientific mass flow controller) and vented into a Shimadzu GC-2014 gas chromatograph (GC) equipped with a combination of molecular sieves (5A), HayeSep Q, HayeSep T, and HayeSep N columns.[49,61] A thermal conductivity detector (TCD) was mainly used to quantify the H_2 concentration, and a flame ionization detector (FID) with a methanizer was used to quantitatively analyse the CO content and/or any other alkane species. The detectors are calibrated by two different concentrations (H_2: 100 and 1042 ppm; CO: 100 and 496.7 ppm) of standard gases. The gas products were sampled after a continuous electrolysis of ~15 min under each potential. The partial current density for a given gas product was calculated as below:

$$j_i = x_i \times v \times \frac{n_i F p_0}{RT} \times (\text{electrode area})^{-1}$$

where x_i is the volume fraction of a certain product determined by online GC referenced to calibration curves from two standard gas samples (Scott and Airgas), v is the flow rate of 50 sccm, n_i is the number of electrons involved, p_0 = 101.3 kPa, F is the Faradaic constant and R is the gas constant. The corresponding Faradaic efficiency (FE) at each potential is calculated by FE = $j_i/i_{total} \times 100\%$.

Density functional theory calculations

Electronic structure calculations were performed using the Quantum ESPRESSO program package, integrated with the Atomic Simulation Environment (ASE). The electronic wavefunctions were expanded in a series of plane waves with a cutoff energy of 500 eV and an electron density cutoff of 5000 eV. Core electrons were approximated with ultrasoft pseudopotentials. We used the BEEF–vdW exchange–correlation functional, which has been shown to accurately describe chemisorption and physisorption properties on graphene. For adsorption studies, a supercell of lateral size (7 × 7) was used to account for 1% impurity of metal in a graphene lattice, and a vacuum region of at least 18 Å is used to decouple the periodic images. The first Brillouin zone was sampled with (3 × 3 × 1) Monkhorst–Pack *k*-points. All atoms were allowed to relax until the maximum force on each atom was below 0.05 eV $Å^{-1}$ for each calculation. To account for the magnetism of the Ni/Co dopants in the graphene lattice, we applied the model developed by Krasheninnikov *et al.*,[44] for metal dopants at single (M@SV) and double vacancies (M@DV) of graphene layers. All calculations were performed with spin polarization.

The CHE method[62] was used to calculate the free energy levels of all adsorbates. In this model, the chemical potential of

a proton–electron pair equated with that of gas-phase H_2 at 0 V *vs.* RHE, and the electrode potential is taken into account by shifting the electron energy by $-eU$, where e and U are the elementary charge and the electrode potential, respectively. We define the thermodynamic limiting potential of electrochemical reactions to be the negative of the maximum free energy difference between any two successive electrochemical steps. The reaction energies of all individual intermediates are calculated and corrected by zero-point energy (ZPE) and entropy (TS) using the following equation:

$$\Delta G = \Delta E + \Delta \mathrm{ZPE} - T\Delta S$$

We apply the ZPE and $T\Delta S$ values reported by Peterson *et al.*[63]

Author contributions

H. W. designed the experiments of this project. K. J. and H. W. performed material synthesis and catalysis measurements. S. S. designed and performed the DFT calculations. K. J., T. Z., Y. H., S. H., E. S., Y. P., J. D., M. G., D. S., K. A. and H. W. performed material characterization. K. J., S. S. and H. W. wrote the manuscript. All of the authors analyzed the results.

Conflicts of interest

There are no conflicts to declare.

Acknowledgements

This work was supported by the Rowland Fellows Program at Rowland Institute, Harvard University. This work was performed in part at the Center for Nanoscale Systems (CNS), a member of the National Nanotechnology Infrastructure Network (NNIN), which was supported by the National Science Foundation under NSF award no. ECS-0335765. CNS is part of Harvard University. Some of the XAS experiments described in this paper were performed at the Canadian Light Source, which is supported by NSERC, the National Research Council Canada, the Canadian Institutes of Health Research, the Province of Saskatchewan, Western Economic Diversification Canada, and the University of Saskatchewan. This research used resources of the 8-ID (ISS) beamline of the National Synchrotron Light Source II, and the Center for Functional Nanomaterials, U.S. Department of Energy (DOE) Office of Science User Facilities operated for the DOE Office of Science by Brookhaven National Laboratory under Contract No. DE-SC0012704.

Notes and references

1 N. S. Lewis and D. G. Nocera, *Proc. Natl. Acad. Sci. U. S. A.*, 2006, **103**, 15729–15735.
2 A. M. Appel, J. E. Bercaw, A. B. Bocarsly, H. Dobbek, D. L. DuBois, M. Dupuis, J. G. Ferry, E. Fujita, R. Hille, P. J. A. Kenis, C. A. Kerfeld, R. H. Morris, C. H. F. Peden, A. R. Portis, S. W. Ragsdale, T. B. Rauchfuss, J. N. H. Reek, L. C. Seefeldt, R. K. Thauer and G. L. Waldrop, *Chem. Rev.*, 2013, **113**, 6621–6658.
3 C. Costentin, M. Robert and J. M. Saveant, *Chem. Soc. Rev.*, 2013, **42**, 2423–2436.
4 S. Verma, B. Kim, H. Jhong, S. C. Ma and P. J. A. Kenis, *ChemSusChem*, 2016, **9**, 1972–1979.
5 D. D. Zhu, J. L. Liu and S. Z. Qiao, *Adv. Mater.*, 2016, **28**, 3423–3452.
6 D. G. Nocera, *Acc. Chem. Res.*, 2017, **50**, 616–619.
7 S. Chu, Y. Cui and N. Liu, *Nat. Mater.*, 2017, **16**, 16–22.
8 Y. Hori, H. Wakebe, T. Tsukamoto and O. Koga, *Electrochim. Acta*, 1994, **39**, 1833–1839.
9 Y. H. Chen, C. W. Li and M. W. Kanan, *J. Am. Chem. Soc.*, 2012, **134**, 19969–19972.
10 K. P. Kuhl, T. Hatsukade, E. R. Cave, D. N. Abram, J. Kibsgaard and T. F. Jaramillo, *J. Am. Chem. Soc.*, 2014, **136**, 14107–14113.
11 M. Ma, B. J. Trzesniewski, J. Xie and W. A. Smith, *Angew. Chem., Int. Ed.*, 2016, **55**, 9748–9752.
12 M. Liu, Y. Pang, B. Zhang, P. De Luna, O. Voznyy, J. Xu, X. Zheng, C. T. Dinh, F. Fan, C. Cao, F. P. de Arquer, T. S. Safaei, A. Mepham, A. Klinkova, E. Kumacheva, T. Filleter, D. Sinton, S. O. Kelley and E. H. Sargent, *Nature*, 2016, **537**, 382–386.
13 M. B. Ross, C. T. Dinh, Y. Li, D. Kim, P. De Luna, E. H. Sargent and P. D. Yang, *J. Am. Chem. Soc.*, 2017, **139**, 9359–9363.
14 S. Back, M. S. Yeom and Y. Jung, *ACS Catal.*, 2015, **5**, 5089–5096.
15 S. Zhang, P. Kang and T. J. Meyer, *J. Am. Chem. Soc.*, 2014, **136**, 1734–1737.
16 P. P. Sharma, J. J. Wu, R. M. Yadav, M. J. Liu, C. J. Wright, C. S. Tiwary, B. I. Yakobson, J. Lou, P. M. Ajayan and X. D. Zhou, *Angew. Chem., Int. Ed.*, 2015, **54**, 13701–13705.
17 M. Schreier, L. Curvat, F. Giordano, L. Steier, A. Abate, S. M. Zakeeruddin, J. Luo, M. T. Mayer and M. Grätzel, *Nat. Commun.*, 2015, **6**, 7326.
18 J. Wu, S. Ma, J. Sun, J. I. Gold, C. Tiwary, B. Kim, L. Zhu, N. Chopra, I. N. Odeh, R. Vajtai, A. Z. Yu, R. Luo, J. Lou, G. Ding, P. J. Kenis and P. M. Ajayan, *Nat. Commun.*, 2016, **7**, 13869.
19 S. Gao, Y. Lin, X. Jiao, Y. Sun, Q. Luo, W. Zhang, D. Li, J. Yang and Y. Xie, *Nature*, 2016, **529**, 68–71.
20 M. Schreier, F. Heroguel, L. Steier, S. Ahmad, J. S. Luterbacher, M. T. Mayer, J. S. Luo and M. Gratzel, *Nat. Energy*, 2017, **2**, 17087.
21 D. Kim, C. S. Kley, Y. Li and P. Yang, *Proc. Natl. Acad. Sci. U. S. A.*, 2017, **114**, 10560–10565.
22 L. Dai, Q. Qin, P. Wang, X. J. Zhao, C. Y. Hu, P. X. Liu, R. X. Qin, M. Chen, D. H. Ou, C. F. Xu, S. G. Mo, B. H. Wu, G. Fu, P. Zhang and N. F. Zheng, *Sci. Adv.*, 2017, **3**, e1701069.
23 K. Niu, Y. Xu, H. Wang, R. Ye, H. L. Xin, F. Lin, C. Tian, Y. Lum, K. C. Bustillo, M. M. Doeff, M. T. M. Koper, J. Ager, R. Xu and H. Zheng, *Sci. Adv.*, 2017, **3**, e1700921.
24 X. F. Yang, A. Q. Wang, B. T. Qiao, J. Li, J. Y. Liu and T. Zhang, *Acc. Chem. Res.*, 2013, **46**, 1740–1748.
25 A. S. Varela, N. R. Sahraie, J. Steinberg, W. Ju, H. S. Oh and P. Strasser, *Angew. Chem., Int. Ed.*, 2015, **54**, 10758–10762.
26 H. Fei, J. Dong, M. J. Arellano-Jimenez, G. Ye, N. Dong Kim, E. L. Samuel, Z. Peng, Z. Zhu, F. Qin, J. Bao, M. J. Yacaman,

P. M. Ajayan, D. Chen and J. M. Tour, *Nat. Commun.*, 2015, **6**, 8668.
27 D. H. Deng, X. Q. Chen, L. Yu, X. Wu, Q. F. Liu, Y. Liu, H. X. Yang, H. F. Tian, Y. F. Hu, P. P. Du, R. Si, J. H. Wang, X. J. Cui, H. B. Li, J. P. Xiao, T. Xu, J. Deng, F. Yang, P. N. Duchesne, P. Zhang, J. G. Zhou, L. T. Sun, J. Q. Li, X. L. Pan and X. H. Bao, *Sci. Adv.*, 2015, **1**, e1500462.
28 C. M. Zhao, X. Y. Dai, T. Yao, W. X. Chen, X. Q. Wang, J. Wang, J. Yang, S. Q. Wei, Y. E. Wu and Y. D. Li, *J. Am. Chem. Soc.*, 2017, **139**, 8078–8081.
29 H. Nishihara, T. Hirota, K. Matsuura, M. Ohwada, N. Hoshino, T. Akutagawa, T. Higuchi, H. Jinnai, Y. Koseki, H. Kasai, Y. Matsuo, J. Maruyama, Y. Hayasaka, H. Konaka, Y. Yamada, S. Yamaguchi, K. Kamiya, T. Kamimura, H. Nobukuni and F. Tani, *Nat. Commun.*, 2017, **8**, 109.
30 K. Jiang, S. Siahrostami, A. J. Akey, Y. Li, Z. Lu, J. Lattimer, Y. Hu, C. Stokes, M. Gangishetty, G. Chen, Y. Zhou, W. Hill, W.-B. Cai, D. C. Bell, K. Chan, J. K. Nørskov, Y. Cui and H. Wang, *Chem*, 2017, **3**, 950–960.
31 W. Ju, A. Bagger, G.-P. Hao, A. S. Varela, I. Sinev, V. Bon, B. Roldan Cuenya, S. Kaskel, J. Rossmeisl and P. Strasser, *Nat. Commun.*, 2017, **8**, 944.
32 X. Li, W. Bi, M. Chen, Y. Sun, H. Ju, W. Yan, J. Zhu, X. Wu, W. Chu, C. Wu and Y. Xie, *J. Am. Chem. Soc.*, 2017, **139**, 14889–14892.
33 N. Lopez, T. V. W. Janssens, B. S. Clausen, Y. Xu, M. Mavrikakis, T. Bligaard and J. K. Norskov, *J. Catal.*, 2004, **223**, 232–235.
34 M. Valden, X. Lai and D. W. Goodman, *Science*, 1998, **281**, 1647–1650.
35 B. Yoon, H. Hakkinen, U. Landman, A. S. Worz, J. M. Antonietti, S. Abbet, K. Judai and U. Heiz, *Science*, 2005, **307**, 403–407.
36 C. T. Campbell, *Nat. Chem.*, 2012, **4**, 597–598.
37 M. Beley, J. P. Collin, R. Ruppert and J. P. Sauvage, *J. Am. Chem. Soc.*, 1986, **108**, 7461–7467.
38 Y. Wu, B. Rudshteyn, A. Zhanaidarova, J. D. Froehlich, W. Ding, C. P. Kubiak and V. S. Batista, *ACS Catal.*, 2017, **7**, 5282–5288.
39 M. Kuehnel, C. Sahm, G. Neri, J. R. Lee, K. Orchard, A. J. Cowan and E. Reisner, *Chem. Sci.*, 2018, DOI: 10.1039/C7SC04429A.
40 S. Lin, C. S. Diercks, Y. B. Zhang, N. Kornienko, E. M. Nichols, Y. B. Zhao, A. R. Paris, D. Kim, P. Yang, O. M. Yaghi and C. J. Chang, *Science*, 2015, **349**, 1208–1213.
41 N. Kornienko, Y. B. Zhao, C. S. Kiley, C. H. Zhu, D. Kim, S. Lin, C. J. Chang, O. M. Yaghi and P. D. Yang, *J. Am. Chem. Soc.*, 2015, **137**, 14129–14135.
42 X. Zhang, Z. Wu, X. Zhang, L. Li, Y. Li, H. Xu, X. Li, X. Yu, Z. Zhang, Y. Liang and H. Wang, *Nat. Commun.*, 2017, **8**, 14675.
43 D. H. Deng, K. S. Novoselov, Q. Fu, N. F. Zheng, Z. Q. Tian and X. H. Bao, *Nat. Nanotechnol.*, 2016, **11**, 218–230.
44 A. V. Krasheninnikov, P. O. Lehtinen, A. S. Foster, P. Pyykkö and R. M. Nieminen, *Phys. Rev. Lett.*, 2009, **102**, 126807.
45 P. Su, K. Iwase, S. Nakanishi, K. Hashimoto and K. Kamiya, *Small*, 2016, **12**, 6083–6089.
46 F. Lei, W. Liu, Y. Sun, J. Xu, K. Liu, L. Liang, T. Yao, B. Pan, S. Wei and Y. Xie, *Nat. Commun.*, 2016, **7**, 12697.
47 J. A. Rodríguez-Manzo, O. Cretu and F. Banhart, *ACS Nano*, 2010, **4**, 3422–3428.
48 T. Hatsukade, K. P. Kuhl, E. R. Cave, D. N. Abram and T. F. Jaramillo, *Phys. Chem. Chem. Phys.*, 2014, **16**, 13814–13819.
49 K. Jiang, H. Wang, W. B. Cai and H. T. Wang, *ACS Nano*, 2017, **11**, 6451–6458.
50 B. A. Rosen, A. Salehi-Khojin, M. R. Thorson, W. Zhu, D. T. Whipple, P. J. A. Kenis and R. I. Masel, *Science*, 2011, **334**, 643–644.
51 H.-R. M. Jhong, F. R. Brushett and P. J. A. Kenis, *Adv. Energy Mater.*, 2013, **3**, 589–599.
52 R. B. Kutz, Q. M. Chen, H. Z. Yang, S. D. Sajjad, Z. C. Liu and I. R. Masel, *Energy Technol.*, 2017, **5**, 929–936.
53 Y. Lum, Y. Kwon, P. Lobaccaro, L. Chen, E. L. Clark, A. T. Bell and J. W. Ager, *ACS Catal.*, 2016, **6**, 202–209.
54 A. P. Grosvenor, M. C. Biesinger, R. S. Smart and N. S. McIntyre, *Surf. Sci.*, 2006, **600**, 1771–1779.
55 M. Shalom, D. Ressnig, X. F. Yang, G. Clavel, T. P. Fellinger and M. Antonietti, *J. Mater. Chem.*, 2015, **3**, 8171–8177.
56 S. F. Pei and H. M. Cheng, *Carbon*, 2012, **50**, 3210–3228.
57 V. Lee, L. Whittaker, C. Jaye, K. M. Baroudi, D. A. Fischer and S. Banerjee, *Chem. Mater.*, 2009, **21**, 3905–3916.
58 C. Shi, H. A. Hansen, A. C. Lausche and J. K. Norskov, *Phys. Chem. Chem. Phys.*, 2014, **16**, 4720–4727.
59 B. Hinnemann, P. G. Moses, J. Bonde, K. P. Jørgensen, J. H. Nielsen, S. Horch, I. Chorkendorff and J. K. Nørskov, *J. Am. Chem. Soc.*, 2005, **127**, 5308–5309.
60 P. Sabatier, *La catalyse en chimie organique*, Librairie Polytechnique, Paris et Liège, 1920.
61 K. Jiang, R. B. Sandberg, A. J. Akey, X. Liu, D. C. Bell, J. K. Nørskov, K. Chan and H. Wang, *Nat. Catal.*, 2018, **1**, 111–119.
62 J. K. Nørskov, J. Rossmeisl, A. Logadottir, L. Lindqvist, J. R. Kitchin, T. Bligaard and H. Jonsson, *J. Phys. Chem. B*, 2004, **108**, 17886–17892.
63 A. A. Peterson, F. Abild-Pedersen, F. Studt, J. Rossmeisl and J. K. Norskov, *Energy Environ. Sci.*, 2010, **3**, 1311–1315.